A Process/Machine coupling approach: Application to Robotized Incremental Sheet Forming

Jérémy Belchior, Lionel Leotoing, Dominique Guines, Eric Courteille, Patrick Maurine

A Process/Machine coupling approach: application to Robotized Incremental Sheet Forming

J. Belchior[a,*], L. Leotoing[a], D. Guines[a], E. Courteille[a], P. Maurine[a]

[a] *Université Européenne de Bretagne, INSA-LGCGM EA-3913, 20 Avenue des Buttes de Coësmes, 35043, Rennes Cedex, France*

Abstract

In this paper, a Process/Machine coupling approach applied to Robotized Incremental Sheet Forming (RISF) is presented. This approach consists in coupling a Finite Element Analysis (FEA) of the process with an elastic modelling of the robot structure to improve the geometrical accuracy of the formed part. The FEA, assuming a rigid machine, is used to evaluate the forces at the interface between the tool and the sheet during the forming stage. These forces are used as input data for the elastic model, to predict and correct the tool path deviations. In order to make the tool path correction more effective, the weight of three numerical and material parameters of the FEA on the predicted forces is investigated. Finally, the proposed method is validated by the comparison of the numerical and experimental tool paths and geometries obtained with or without correction of the tool path.

Keywords: incremental sheet forming, FE simulation, robot machining, off-line compensation

1. Introduction

The Incremental Sheet Forming (ISF) is an innovative process for small series production and prototyping. The sheet is deformed locally by successive paths of a simple tool, usually a hemispherical punch. Complex shapes can be realized without dies which represents a significant cost benefit. In order to reduce manufacturing costs and improve production versatility, serial robots can be used for industrial processes like the ISF. For example, Meier et al. [2009a] have coupled two industrial robots to perform

*Corresponding author

Email addresses: jeremy.belchior@insa-rennes.fr Tel.: +33 (0) 223238516 (J. Belchior), lionel.leotoing@insa-rennes.fr (L. Leotoing), dominique.guines@insa-rennes.fr (D. Guines), eric.courteille@insa-rennes.fr (E. Courteille), patrick.maurine@insa-rennes.fr (P. Maurine)

two point incremental forming. The first robot moves the forming tool in depth direction and along the contour path. The second robot drives a supporting tool to hold the sheet on the backside. For the same purpose Vihtonen et al. [2008] have used a serial robot and an appropriate clamping device. Nevertheless robot serial structure presents high compliances and a low absolute positioning accuracy. The process forces acting on the tool lead to robot structure deflection and then to tool path errors. To compensate the tool path errors induce by the machine (robot) and/or the process compliance different approaches are available in the literature.

Bres et al. [2010] give a solution that consists in the dynamic elastic modelling of the machine or the robot structure in order to compensate by a linear or non linear feedback control the elastic deformations of the structure that degrade the TCP (Tool Center Point) pose accuracy. Outputs of such control consist in modifying the actuator torques. However Bigras et al. [2007] have shown that its implementation is difficult in actual industrial robots where only the TCP pose is controlled. Moreover, the dynamic parameters (inertia, center of gravity, gear ratio) must be identified by dedicated methodologies such as proposed by Khalil and Dombre [2002] or de Wit et al. [1996].

For flexible processes as ISF a promising solution consists in using a robust closed-loop control of the machine. For those processes, dedicated sensors as stereovision cameras, lasers, etc. can be involved to perform an on-line feedback control of the part geometry during the process. However the setup of the machine control parameters requires an appropriate and realistic process model that can be difficult to obtain. This can be done for example from a set of spatial impulse responses measured by linearization around a pre-planned tool path as explained by Allwood et al. [2009] and by Music and Allwood [2012]. As proposed by Rauch et al. [2009] it is also possible to use on-line measurements available directly on the machine itself (values of the encoders and/or torques) as a feedback to achieve a real time closed-loop control. To overcome the difficulties related to the previous approaches, one solution is based on realistic parametric models of machines and robots to predict the elastic deformations. The methodologies proposed in the literature are based either on lumped-parameter model in Dumas et al. [2011] or more realistic Finite Element models as in Marie and Maurine

[2008]. Since outputs of these models are TCP pose errors, the term elasto-geometrical model is used. As a result, a correction of the tool path deviations is possible and can be easily implemented in the native programming language of the controller (real-time or off-line programming).

With this second approach, the knowledge of the forces acting on the TCP is essential. Several studies, such as Ambrogio et al. [2007], Jeswiet et al. [2005], Petek et al. [2005], have analysed the influence of experimental setup parameters on the prediction of the forming forces. Duflou et al. [2007a] proposed a force prediction model applied during the forming of a cone as a function of the step-down amplitude, the wall angle, the tool diameter and the sheet thickness. This model, based on a simple regression equation, could predict the peak, steady-state and in-plane forces with a high degree of confidence. Nevertheless this analytical model is only valid for simple geometries. For more complex geometries, Aerens et al. [2010] involve the previous model. A strategy, based on experimental measurements, is proposed to identify the model parameters. Several materials were tested. For each material, an analytical formula able to predict level of the steady-state tool force is fitted for various parts. The ultimate tensile strength of the considered material seems to govern the level of the steady-state force. Due to the complex tool path in the ISF process, the most common way to estimate these forces is based on a FEA of the process. Meier et al. [2011] have proposed a model-based approach in which a MBS (Multi Body System) model of the robot is coupled with a FEA of an ISF operation. In the MBS model, the links are assumed rigid and the elastic behavior of the robot structure is described considering only the joint stiffness. In fact this coupling approach has not been really carried out since measured forces during a first run without any compensation have been defined as the input data of the robot model instead of using the predicted forces calculated with FEA model. To avoid errors due to possible inaccuracies in the force prediction from analytical or numerical models, Verbert et al. [2009] have chosen the same strategy. As explained by the authors, the main drawback of this procedure is that the forming of a dummy part is required. The hypotheses used in the FEA of the process made by Meier et al. [2009b] can explain the inaccuracies of the numerical model and finally the choice

of this strategy. With these hypotheses the simulated forces through the forming of a straight groove present a maximum overestimation of 30% compared to the measured ones. This result underlines the difficulty to accurately compute the forces induced by the process.

The FEA of the ISF operation is commonly applied to predict the final geometry of the part. Most studies on the simulation of the ISF like the one from Ambrogio et al. [2004] are based on the same hypotheses: thin shell elements, frictionless conditions between the tool and the sheet, rigid tool, hardening power law, encastre boundary conditions for the clamping system... These models are usually effective to predict the final shape but when results of force prediction are presented, they are systematically overestimated. In the literature, this overestimation is usually justified by three main factors described below:

- The first one concerns the deformation mechanisms during the process which are not well identified. Eyckens et al. [2009] have shown that Through-Thickness Shear (TTS) appears by measuring small deformed holes in cone wall angles. Emmens and van den Boogaard [2009] have demonstrated that this shear can delay the onset of necking and may explain the high levels of deformation in ISF (strain levels of about 70%-120% can be reached). Allwood and Shouler [2007] demonstrate, in a simplified version of incremental forming, that the through-thickness shear is significant in the direction of the tool movement. In Allwood and Shouler [2009], TTS is incorporated into Marciniak-Kuczynski model and it is shown that the forming limit curve increases with increasing TTS. Henrard et al. [2011] have recently studied the ability of FEA to predict the correct tool force during a Single Point Incremental Forming (SPIF) operation. The forming of two frustum cones with different wall angles (20° and 60°) has been simulated to compare the effects of various numerical and material parameters. TTS can be neglected for the 20° cone, while it is significant for the 60° cone. Two different types of element were chosen for the simulation of each geometry: shell elements neglecting TTS, and brick elements modelling TTS. For the 60° cone, the error between the experimental and simulated values is reduced from 40% to 20%

when the TTS is considered with the brick elements.

- The second factor which can influence the level of the simulated forming forces is the modelling of the plastic behavior of the sheet material. The calibration of the hardening law is one of the most influent on the force level. Indeed hardening laws are typically identified from tensile test until a level of strain which is about 20% whereas the level of strain reached during the process can be 2 or 3 times greater. In Flores et al. [2007], a strong discrepancy between the simulation force prediction based on an elastic-plastic law with isotropic or kinematic hardening model is observed. For a AA3003-O, a decrease of 20% of the predicted forces is observed when kinematic hardening is introduced in the FE simulation of a frustum cone with a wall angle of 50° . But recently, Henrard et al. [2011] have also compared the influence of several plastic behavior (Swift and Voce hardening laws, isotropic or kinematic hardening models, isotropic von Mises and the anisotropic Hill yield criteria) on the force prediction. The forming material is also an aluminium alloy (AA3003-O). It is shown that, for this material and for important wall angle (60°) cone, leading to accumulated equivalent engineering strain of about 200%, the choice of isotropic or anisotropic yield locus is negligible. Moreover, an isotropic saturating law such as Voce's seems the most suitable hardening behavior. A difference of about 20% on the axial force is observed between the Voce and Swift hardening laws. An other conclusion of this study, is that the kinematic hardening behavior appears to have only a little effect on the force prediction for this material. As one can see it, this point remains debatable but for the 5086 aluminum alloy considered in this study, the hardening is mainly isotropic and the contribution of the kinematic hardening is low and will be neglected in this study.

- Finally the boundary conditions applied to the simulation (modelling of the clamping system) can also lead to an artificial stiffening of the model as it has been remarked by Bouffioux et al. [2007]. To avoid the force overestimation due to encastre boundary conditions, the clamping system has been modeled by

springs distributed along the sheet edges. The nodes of the edges are fixed in rotation and in translation following the axial tool direction while the displacements in the sheet plan are possible and depend on the stiffness springs. To correlate with experimental force values, a unique spring stiffness has been computed using an inverse method based on an indentation test.

With the aim to reduce the process time and to propose a simplified method, an off-line compensation procedure based on an elastic modelling of the machine structure coupled with a FEA of the process, is proposed in this work. The SPIF procedure and the process parameters are firstly described. An experimental investigation studies the robot ability during the forming of a frustum cone by comparing the experimental results from a three axis milling machine and the robot. Due to the high stiffness of its structure, the measured forces on the milling machine are defined as a reference. Then, a FE model of the process is proposed and the force prediction of this model is numerically investigated. Finally, the predicted force is used as an input data of the robot elastic model in order to compute tool path correction of the robot. The effectiveness of the proposed method is verified by comparing the nominal and the measured tool path. This approach is finally validated on a non-symmetrical geometry: a twisted pyramid.

2. Process description

2.1. Part and tools

The part consists of a frustum cone of $45°$ wall angle centered on a sheet of $200 \times 200 \times 1\ mm^3$ (Figure 1). The depth of the frustum cone is 40 mm. The chosen material is an 5086 H111 aluminum alloy. The forming tool is a hemispherical punch with a $15\ mm$ diameter. The feed rate value of the tool is $2\ m/min$ and the tool rotation is locked. Grease is not an ideal lubricant but it has been used to reduce the friction coefficient between the sheet and the tool. The clamping system is composed of a blank holder screwed on a rigid frame (Figure 2).

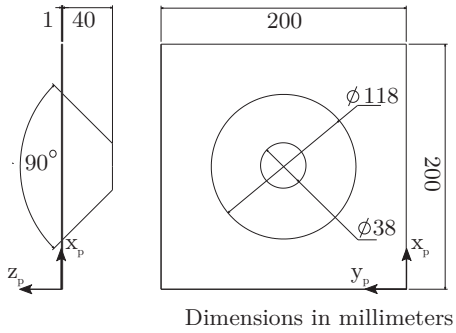

Figure 1: Shape of the frustum cone (45° wall angle)

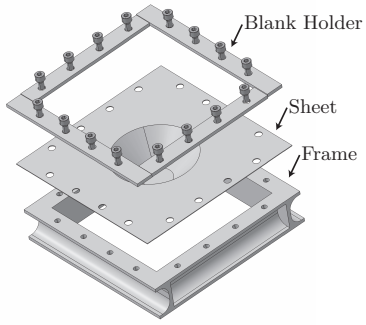

Figure 2: Clamping system

2.2. Process parameters

The incremental step direction is along $\mathbf{z}_p$ (Figure 3). The trajectory consists of successive circular tool paths at constant $\mathbf{z}_p$. The incremental step size value (Δ_Z) is 1 mm per loop. Different strategies to perform a frustum cone in SPIF are available in the literature (multi-pass, begin the forming at the center of the sheet...) and their application leads to different results in term of geometrical accuracy. However, our first objective is to correct the errors due to the low stiffness of serial robots. These errors will appear whatever the forming strategy. In consequence, a classical strategy has been chosen for the study in order to build a generic method applicable for all the forming strategies.

2.3. Measurement systems

The forces acting on the tool are measured using a six-component force cell (ATI Omega 190). The three orthogonal components of the forming force F_x, F_y, F_z (see

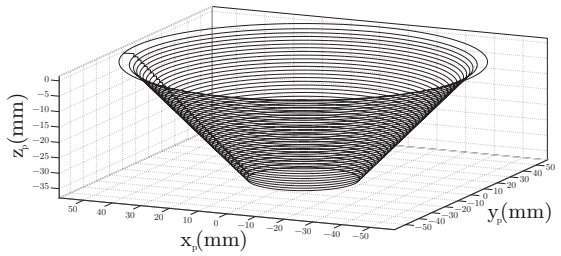

Figure 3: Target tool path - successive circular paths - Δ_Z=1 mm

Figure 1) are used in this study. The force F_z is the axial force applied in the axial direction of the tool whereas the other two components F_x and F_y, located in the xy-plane, evolve as sinusoidal signals. During the forming process the real tool path is measured by a Nikon Metrology K600-10 photogrammetric measurement system. This system has a pose measuring accuracy of $\pm$ 37 μm for a single point. After the forming process the part geometry is measured by a coordinate-measuring machine (CMM). The tactile measurement of the machine presents an accuracy of $\pm$ 3.5 μm for a single point.

2.4. Forming machines

In order to evaluate the ability of an industrial serial robot (Fanuc S420iF) to form a part with ISF process, a comparison of the experimental results obtained from a three axis milling machine (Famup MCX500) and the robot is made. The milling machine is a three axis cartesian structure. It can develop up to 7000 N at the extremity of the tool with a precision of $\pm$ 15 μm. Due to the high stiffness of the cartesian structure of the milling machine, the errors on the tool path induced by the elastic deformations of the machine can be neglected. Consequently, the experimental results obtained with this machine will be considered as the reference. The robot has a payload capacity of 1200 N. Its kinematic closed loop increases the global stiffness of the structure. Its maximum accuracy error with a load of 650 N applied on the TCP is about 3.2 mm. The clamping system is fixed on a rigid table near the robot base to maximize the stiffness of the robot during the process (Figure 4).

To show the weight of the robot stiffness on the forming force, the static equilibrium of the tool, during the process, is presented. Because feed rates are closed to 1 m/mn

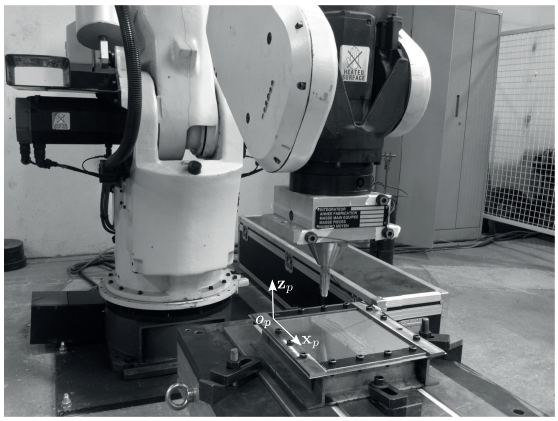

Figure 4: Fanuc robot S420iF with the experimental set-up

the process can be considered as quasi-static. It is assumed that the tool is always in contact with the sheet. The gravity and the friction are neglected. $\mathbf{F}_{S/R}$ is the wrench exerted by the sheet on the robot (Eq. 1) and $\mathbf{F}_{R/S}$ is the wrench exerted by the robot on the sheet (Eq. 2).

$$\mathbf{F}_{S/R} = \mathbf{K}_S.(\mathbf{P}_R - \mathbf{P}_0) \tag{1}$$

$$\mathbf{F}_{R/S} = \mathbf{K}_R.(\mathbf{P}_R - \mathbf{P}_T) \tag{2}$$

Where:

- $\mathbf{P}_0 = [P_{0x}, P_{0y}, P_{0z}, R_{0x}, R_{0y}, R_{0z}]^T{}_{(\mathbf{O_p}, \mathbf{x_p}, \mathbf{y_p}, \mathbf{z_p})}$ is the initial pose of the contact point between the tool and the sheet (Figure 5).
- $\mathbf{P}_R$ is the pose actually reached by the TCP without correction.
- $\mathbf{P}_T$ is the targeted pose.
- $\mathbf{K}_S$ is the stiffness matrix (6×6) of the sheet and clamping device which depends on the position and the type of the clamping system, and on the sheet material and process parameters.
- $\mathbf{K}_R$ is the stiffness matrix (6×6) of the robot structure, which depends on the

joint configuration of the robot and on its geometrical and mechanical parameters (joint stiffness, quadratic moments of links,...).

The static equilibrium, at the contact point between the tool and the sheet, gives:

$$\mathbf{F}_{S/R} = \frac{K_S.K_R}{K_S + K_R}.(\mathbf{P}_0 - \mathbf{P}_T) \tag{3}$$

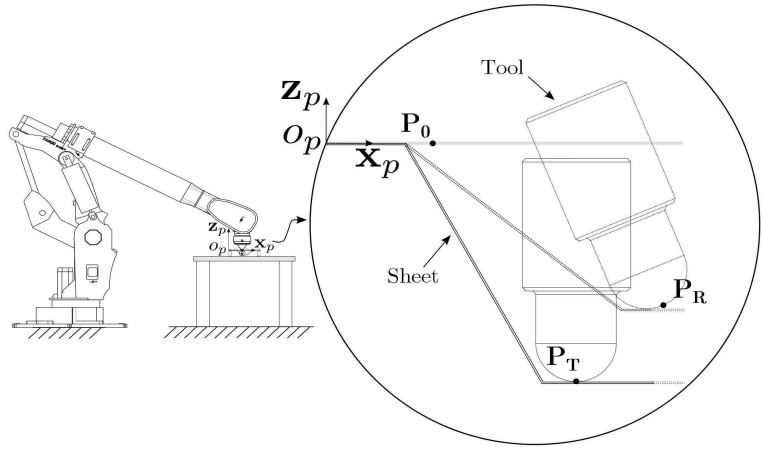

Figure 5: Schematic view of the forming configuration

It means that the lowest stiffness between $\mathbf{K}_R$ and $\mathbf{K}_S$ will have the major impact on the forming force $\mathbf{F}_{S/R}$ and finally on $\mathbf{P}_R$.

2.5. Results

The measured force along the tool axis for both the milling machine and the robot is shown Figure 6. The force components are given as an average per loop. A difference of about $400\ N$ is observed at the end of the trajectory, which represents 30 % of the final value. It shows that the elastic behaviour of the robot has to be considered with the respect to the stiffness of the sheet and the clamping device. The difference between the two final force levels can be explained by the low stiffness of the robot structure which leads to a decrease of the incremental step size value during the forming stage. At the end of the trajectory the real incremental step size value varies from 0.1 to 0.8 mm during a loop which is lower than the constant value (1 mm) applied with the

milling machine. These observations on the forming forces are confirmed by results shown Figure 7. On this figure, the influence of a lower incremental step size on both the final depth and the wall angle of the frustum cone made by the robot is clearly observed. The part is measured along the cut axis before the unclamping of the sheet and the maximum difference between the measured geometries of the part made with the milling machine and the robot is 4 mm. A 2 mm step is considered on the CMM to measure the shape of the robot made part. Due to this discretization, the cut section of the formed part shown Figure 7 is not smooth near the bottom of the part.

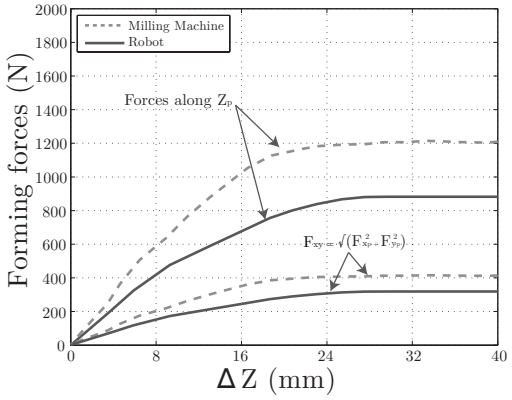

Figure 6: Comparison of the measured force in function of the theoretical depth of the cone (Δ_z).

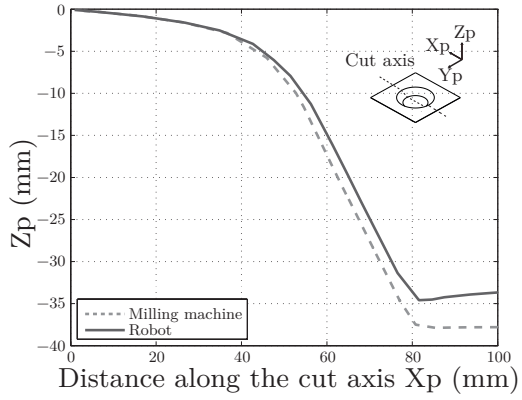

Figure 7: Comparison of the final shape along the cut axis

The tool path error of the robot is depicted in Figure 8. It represents the difference between the nominal trajectory (computed with a CAD software) and the measured

tool path of the robot without correction. For more legibility, the errors along $\mathbf{x}_p$, $\mathbf{y}_p$ and $\mathbf{z}_p$ axis are presented separately in the plane $(\mathbf{O}_p, \mathbf{x}_p, \mathbf{y}_p)$ for the whole tool path respectively on the (Figure 8(a), 8(b), 8(c)). As one can see, a significant TCP deviation can be observed. The maximum errors are about $-5\ mm$, $\pm 3.5\ mm$ and $-5\ mm$ respectively along $\mathbf{x}_p$, $\mathbf{y}_p$ and $\mathbf{z}_p$ directions. The absolute values of the mean errors are about $1\ mm$ along $\mathbf{x}_p$, $\mathbf{y}_p$ and $2.6\ mm$ along $\mathbf{z}_p$ axis. Obviously these errors are not compatible with the process requirements.

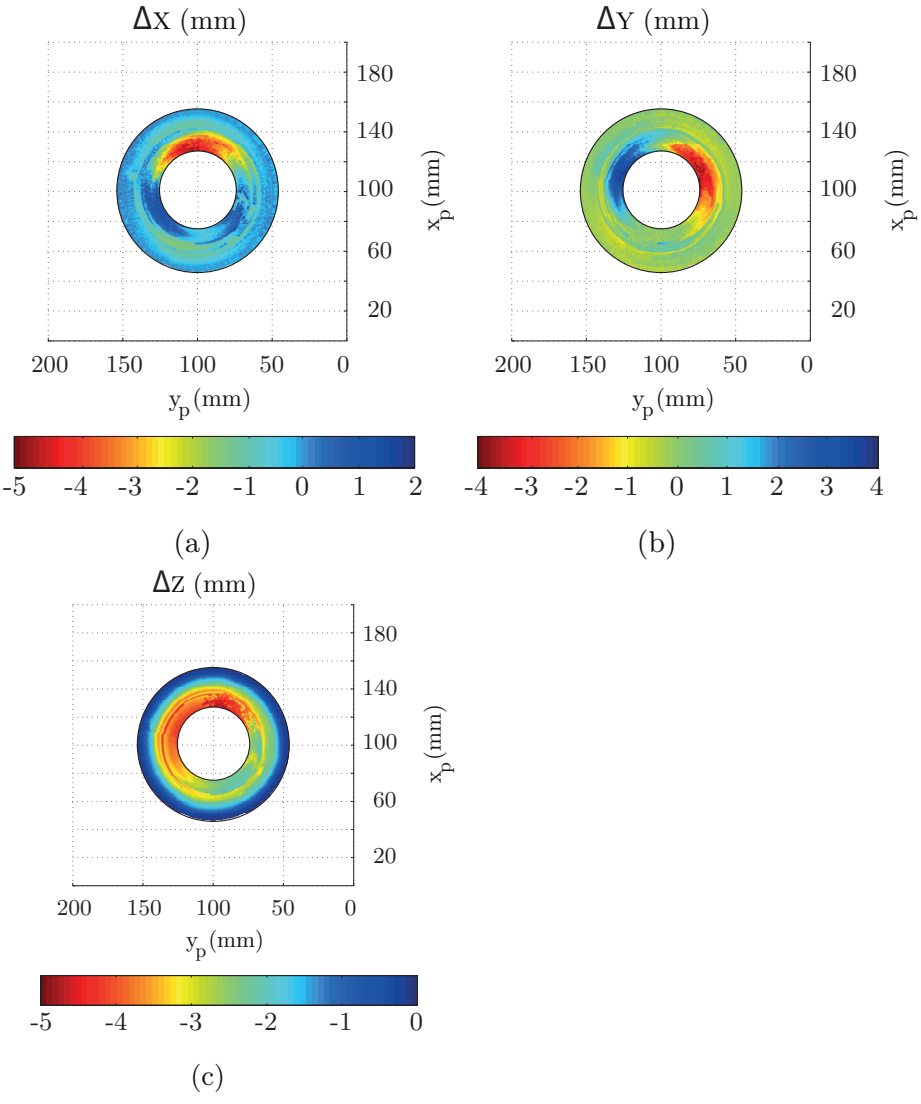

Figure 8: Tool path errors along $\mathbf{x}_p$ (a), $\mathbf{y}_p$ (b) and $\mathbf{z}_p$ (c) without correction (Fanuc S420iF)

3. FE simulation: Improvement of the force prediction

To limit the path error through a coupling approach, a precise force prediction is required. In the literature, the main factors identified like the most important in the forming force prediction by FE simulation are: (i) the choice of the element type, (ii) the consideration of the through thickness shear, (iii) the plastic behavior model of the tested material and finally (iv) the modeling of the boundary conditions applied to the sheet. These different key parameters have been clearly identified in particular in two complete studies on this subject Henrard et al. [2011], Bouffioux et al. [2007]. In sections 3.1 to 3.4, the parameters listed above are presented and discussed and their influence on the force prediction is evaluated through three different FE models numerically investigated in section 3.5.

3.1. Model description

All the numerical simulations are done with the ABAQUS© software using an implicit formulation. A 45° pie model is chosen to minimize the computation time (Figure 9). This approach has been first described by Henrard et al. [2011] and it has been shown that the results of a whole blank and a 45° pie models are very close. In particular, the axial force F_z computed by the partial model is generally lower than the one calculated with the full model but the difference doesn't exceed 10 %. Symmetry boundary conditions are applied on the 0° and 45° sections. The tool path of the 45° pie model is computed with a CAD software (Figure 10). The starting points of each incremental step are defined on the same side. The same z level strategy as the one previously described in section 2.2 is applied.

3.2. Element type and mesh

The meshing size is smaller at the contact point between the tool and the sheet over the trajectory. Two types of elements are compared (S4R and C3D8I). The S4R element is a 4-node, quadrilateral, stress/displacement shell element with reduced integration and a large-strain formulation. It is particularly dedicated for stamping processes of thin shells and allows reduction of the computation time. The C3D8I element

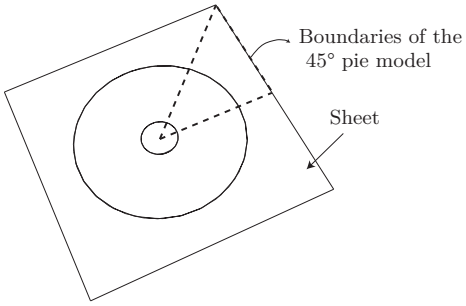

Figure 9: Description of the 45° pie model

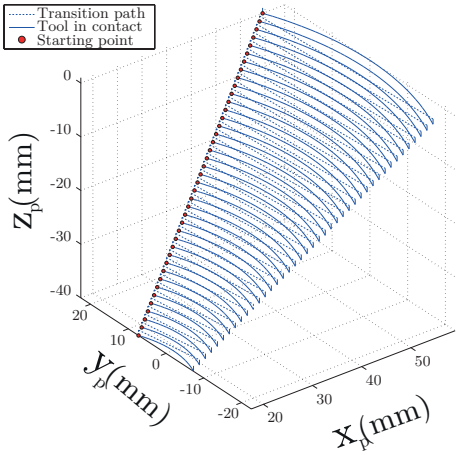

Figure 10: Tool path of the 45° pie model

is a 8-node linear brick with full integration and incompatible modes. By means of a preliminary study, it has been shown that it is sufficient to define four elements to correctly predict the shear in the shell thickness. The main difference between the S4R and the C3D8I elements is the ability of the brick element to model the through thickness shear. When, C3D8I elements are used in the contact zone between the tool and the sheet (Figure 11), S4R elements are kept on the other areas. This 'mix model' leads to a reasonable computation time despite the choice of C3D8I elements. Shear angle values of about 10° in each direction (γ_{13} et γ_{23}) have been noted on the final mesh with 4 brick elements in the shell thickness. Similar values have been obtained by Eyckens et al. [2009].

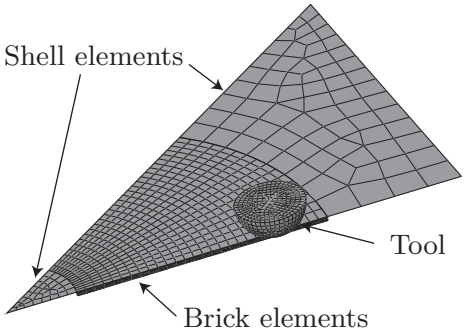

Figure 11: Description of the mix model

3.3. Boundary conditions

In the literature the clamping system is usually modeled as an encastre boundary condition. However sliding between the sheet and the clamping system can appear and reduce the predicted force level. To quantify the clamping system modelling two types of boundary conditions are investigated. The first one consists in defining encastre boundary condition on the four edges of sheet in contact with the clamping system. For the second case the clamping system is modeled by pressure areas applied on the contact zone between the sheet and the blank holder (Figure 12).

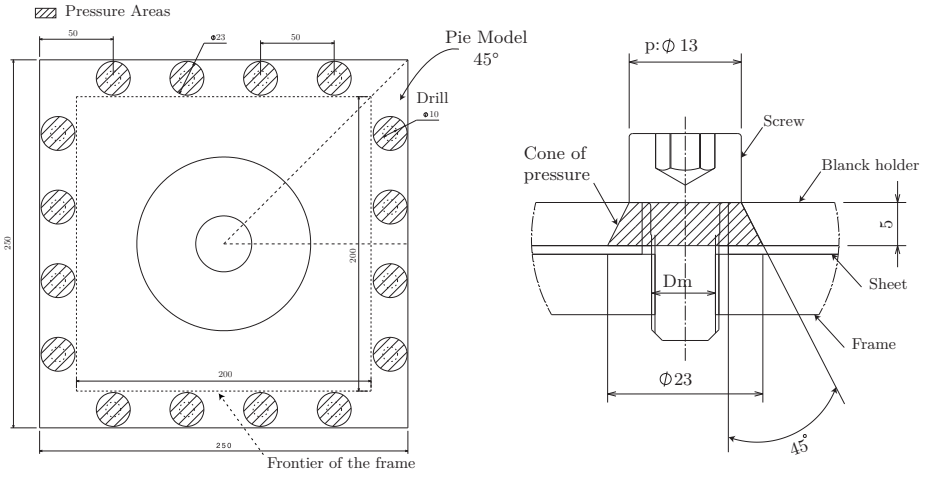

Figure 12: Description and modelling of the clamping system

The pressure (4.3 MPa) applied on each tightening areas, is estimated from the experimental torque applied on each screw (20 Nm) and measured by means of a torque wrench. The contact between the frame and the sheet is modeled with a friction coef-

ficient of 0.05.

3.4. Material behavior

Based on previous works of Zhang et al. [2010], an elasto-plastic model with an isotropic von Mises yield criterion is used to describe the behavior of the 5086 H111 aluminum alloy. It has been shown previously that this material exhibits a quasi-isotropic plane behavior and a low transversal thickness anisotropy. The elastic behavior of the material is defined by the Young modulus E=66 GPa and the Poisson's ratio ν=0.3.

Two different hardening laws are implemented on the model. First a Ludwick law is chosen:

$$\overline{\sigma} = \sigma_e + K_1.\overline{\varepsilon_p}^n \tag{4}$$

where $\overline{\sigma}$ is the equivalent stress, σ_e the initial yield stress (σ_e = 125.88 MPa), $\overline{\varepsilon_p}$ is the equivalent plastic strain, K_1 = 447.08 MPa, n = 0.413.

Secondly a Voce law described by Diot et al. [2006] to model saturation or softening effects of aluminum alloys is applied. The formulation is given by:

$$\overline{\sigma} = \sigma_e + K_2.\sqrt{1 - e^{(-B.\overline{\varepsilon_p})}} \tag{5}$$

with σ_e = 130.2 MPa, K_2 = 330.37 MPa, B = 3.94.

The constants of the two hardening laws defined above are determined from the experimental stress/strain curve of a tensile test made in the rolling direction. This experimental curve and the identified laws are presented in Figure 13.

Due to the high level of deformation reached in the process, the hardening law must be chosen carefully. Figure 13 shows the strain range reached in ISF (up to 120%) in comparison with the strain level reached in the uni-axial tensile test (about 20%). For high levels of deformation, it is difficult to identify accurately the hardening behavior with only a database from a uni-axial tensile test. The choice of the Voce law leads to

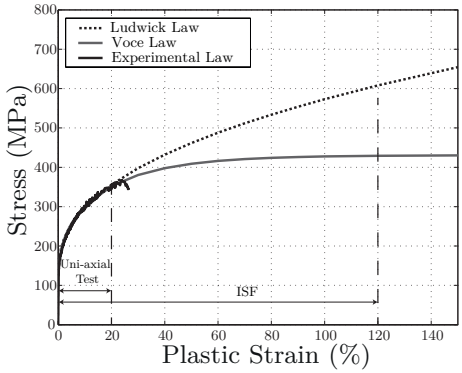

Figure 13: Hardening laws implemented in the simulation

a constant stress for strain higher than 60%. On the contrary the Ludwick law presents a stiffer behavior for large strains.

3.5. Models

Finally, to quantify the influence of each parameter discussed above on the force prediction three different modelling configurations are proposed. The table 1 sums up the different assumptions for each model.

Table 1: Description of the compared models

	Elements	Boundary conditions	Hardening laws
Model 0	Shell	Encastre	Ludwick
Model 1	Brick + Shell	Encastre	Ludwick
Model 2	Brick + Shell	Realistic	Ludwick or Voce

Model 0 is built with the same hypotheses of the literature. Model 1 uses brick elements to model accurately the through thickness shear. Model 2 represents a more realistic clamping system with pressure areas applied on the contact zone between the sheet and the blank holder. Based on Model 2, the weight of the hardening law (Ludwick or Voce) is evaluated. For each model, the predicted force along the tool axis is compared with the experimental force value from the milling machine. This value is defined as the reference since the milling machine is assumed to be perfectly rigid. The mean force at each loop of the trajectory is computed when the TCP crosses the middle axis of the 45° pie model.

3.6. *Influence of TTS*

The importance of TTS on the force prediction is evaluated through the comparison of results from Model 0 and Model 1. It is verified that the force reaches a maximum steady state value according to the work of Duflou et al. [2007b]. The Figure 14 shows that the choice of thin shell elements does not give a good agreement between experimental and predicted force. A maximum difference between Model 0 and experiments of approximately 750 N is identified which represents 40% of the final value. The predictions of Model 1 give better results. With TTS consideration the improvement of the force prediction is about 30%. For that purpose, brick elements have to be considered. Nevertheless the prediction of the final geometry of the part is very close for both elements (Figure 15).

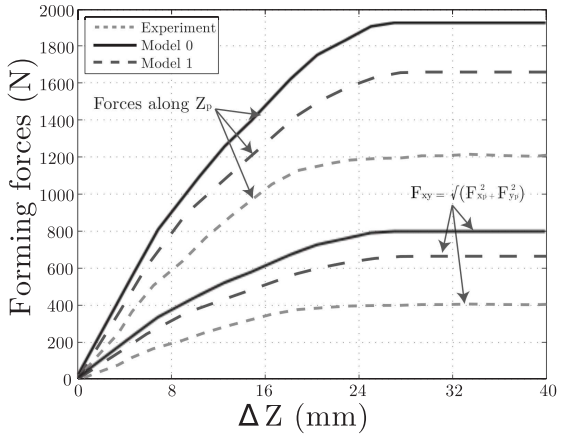

Figure 14: Effect of the finite element type on the force

3.7. *Influence of boundary conditions*

To measure the effect of the boundary conditions, results of Model 1 and Model 2 are compared. The Figure 16 shows a comparison between the simulated forces from the two different boundary conditions. As expected, the more realistic model with the pressure (Model 2) gives a predicted force level lower than Model 1 and closer to the experiments. This modelling improves the force prediction of 55% compared to the Model 1. However, before a value of 20 mm for Δ_Z the predicted forces is lower than the measured one. This difference is linked with a slight sliding during the simulation.

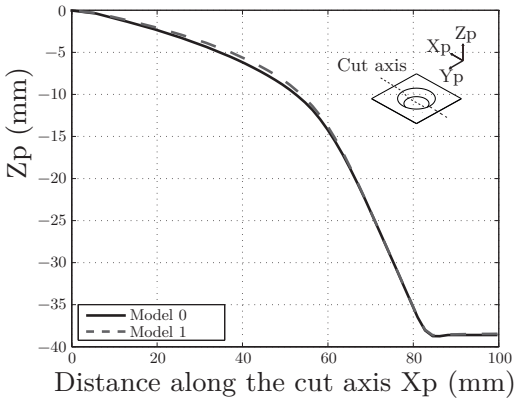

Figure 15: Effect of the finite element type on the final geometry prediction

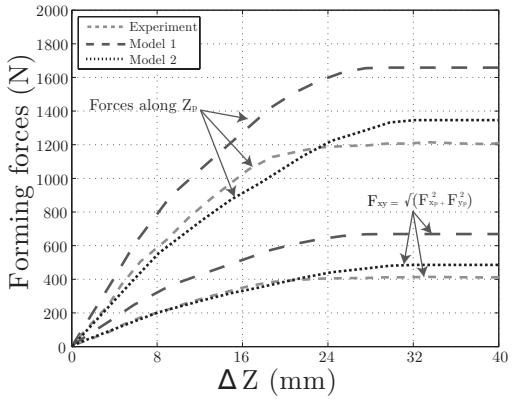

Figure 16: Effect of the clamping model on the force

3.8. Influence of the hardening law

Based on Model 2, the weight of the hardening law (Ludwick and Voce) is evaluated. The maximum reached plastic strain level is about 80% as it is shown in Figure 17. The effects of this choice on the force F_z are depicted in Figure 18. The maximal difference between theses curves is about 150 N which represents 10% of the maximal force value. The Voce law gives a better correlation with experiments than the Ludwick law. Because no experimental setup has been made to identify the hardening law for high levels of deformation, the Voce law is chosen for the application of the correction of the tool path errors.

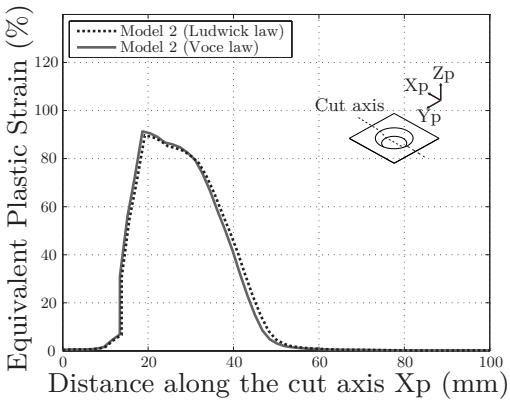

Figure 17: Effect of the hardening law on the final strain prediction

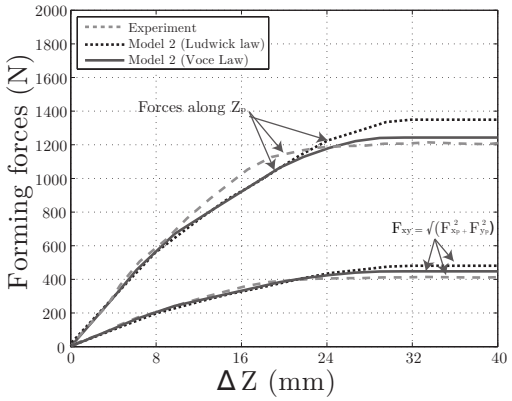

Figure 18: Effect of the hardening law on the force

3.9. Conclusion

From FE investigations presented above, an accurate estimation of both the force magnitude along the tool axis F_z and the xy-plane force F_{xy} has been obtained. This force prediction could be used before performing the coupling approach instead of a force estimation obtained from an analytical model or a first test run made on a stiff machine. The calculation time is about 1 hour for the first model and 6 hours for the last one (Simulation was made using a computer with a 2.33Ghz CPU - 16GB of Ram). If we compare the time and the cost needed to perform the test on a milling machine this strategy can be a good alternative. This method offers also the possibility to be easily included on an optimization loop to improve the forming strategy in order to enhance

the geometrical accuracy of the process. Obviously the time calculation increases when a more complex part which cannot be represented by a symmetrical model is studied but Giraud-Moreau et al. [2013] have shown that remeshing techniques could be an interesting alternative to reduce the computational times. One must be noted that a comparable degree of confidence between experimental and predicted forces has been observed previously by Henrard et al. on a different aluminium alloy.

4. Elastic model of the robot

The elastic modelling of the robot is performed using the analytical method proposed by Deblaise et al. [2006]. This modelling has been already described in the RISF context by Belchior et al. [2013]. It consists in describing the elastic behavior of the robot as a unique elastic beam. The resulting analytical model can be written by:

$$ {}^{0}\Delta_R = \left({}^{0}\mathbf{K}_R\right)^{-1} {}^{0}\mathbf{F}_{R/S} \tag{6} $$

${}^{0}\Delta_R$, ${}^{0}\mathbf{F}_{R/S}$ and ${}^{0}\mathbf{K}_R$ are expressed within the robot base frame $(\mathbf{O_0}, \mathbf{x_0}, \mathbf{y_0}, \mathbf{z_0})$. ${}^{0}\mathbf{F}_{R/S}$ is a 6×1 vector ${}^{0}[F_x\ F_y\ F_z\ M_x\ M_y\ M_z]$ which represents the equivalent wrench acting at the TCP. The components F_x, F_y and F_z are computed by the FE simulation (cf. section 3.8) and M_x=M_y=M_z=0 because the TCP corresponds to the forming tool tip and a point contact with the sheet is assumed. ${}^{0}\Delta_R$ stands for the elastic displacements and ${}^{0}\mathbf{K}_R$ is the equivalent 6×6 stiffness matrix that describes the whole elastic behavior of the robot structure. As explained in Belchior et al. [2013] for each pose of the tool path the joint variables of the robot are computed with its inverse geometrical model and their values are then used to calculate the components of ${}^{0}\mathbf{K}_R$.

To identify the stiffness parameters of the FANUC S420iF structure within the workspace corresponding to the forming application, a set of 150 TCP poses have been generated. A complete characterization of the robot has been obtained by stressing all its joints by means of a cable-pulley device used to generate forces at the end-effector along all axis of the reference frame R_0. The magnitude of the loads applied during this

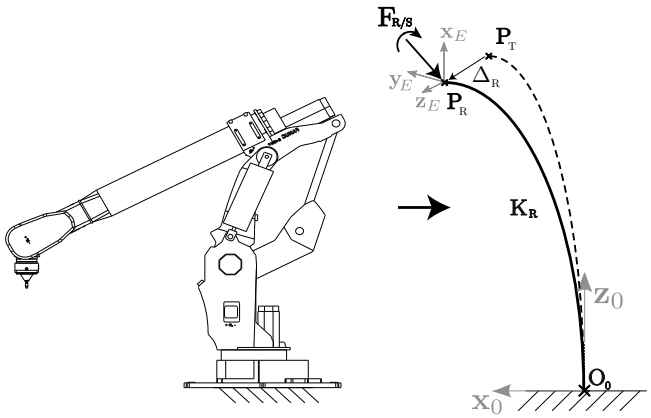

Figure 19: FANUC S420iF modelling

calibration stage was chosen according to the robot payload. The identification phase is performed using a first loading configuration to reach the 150 poses and another loading configuration is chosen for the validation phase. All stiffness parameters of the robot involved in the calculation of the equivalent stiffness matrix ${}^0\mathbf{K}_R$ are identified through a multi-objective optimization procedure based on a genetic algorithm using the software modeFRONTIER©. For the FANUC S420iF, 33 joint stiffness values have to be identified from measured data. The differences between controlled and reached poses have been measured for each level of payload and without to obtain the real elastic displacements. If ${}^0\Delta\mathbf{P}_R^{m,p}$ and ${}^0\Delta\mathbf{P}_R^{c,p}$ stand respectively for the vectors of the measured and calculated displacements for the pose and the load p, the error function is defined by:

$$ {}^0E_R^p = \left\| {}^0\Delta\mathbf{P}_R^{c,p} - {}^0\Delta\mathbf{P}_R^{m,p} \right\| \tag{7} $$

The joint stiffness values gathered in the vector Γ are identified by minimizing, for a set of n_p poses and loads, the following function:

$$ C\left(\Gamma\right) = \sum_{i=1}^{n_p} \sqrt{\left({}^0E_R^p\right)^2} \tag{8} $$

For the forming of the frustum cone previously described the mean computed values of three main components of K_R are $K_{xx} = 937\ N/mm$, $K_{yy} = 597\ N/mm$

and $K_{zz} = 898\ N/mm$. During the forming trajectory, the variation of these ones are respectively $\pm 1.1\%$, $\pm 2.3\%$ and $\pm 3.2\%$. If the stiffness of the robot is kept constant during the process, these fluctuations can represent at the end of the trajectory a variation of the predicted displacement of $\pm$ 0.2 mm. Obviously these variations will increase for larger parts which shows the necessity to compute K_R at each point of the robot tool path.

The identified elastic model allows to predict the TCP displacements induced by elastic behavior of the robot structure over the workspace whatever the load applied on the tool. The prediction maximum and mean errors respectively of $\pm 0.3\ mm$ and $\pm 0.15\ mm$ remain compatible with the process requirements.

5. Coupling approach Process/Machine

This approach consists in coupling the FEA of the forming process and the elastic modelling of the robot. To perform this approach a post-processor is adopted (Figure 20) according to the approach described by Meier et al. [2011]. Using the assumption of a quasi static process, only the elastic behavior of the mechanical structure is considered. Measurements of the TCP elastic displacements have been conducted with the controller on and off (actuators blocked) and have shown exactly the same elastic behavior of the robot. As a result, it has been assumed that the robot controller does not compensate the elastic displacements and do not have to be integrated in the elastic model. The needed data are the process and material parameters and the values of the robot stiffness matrix. The approach is a total off-line method without feedback loop.

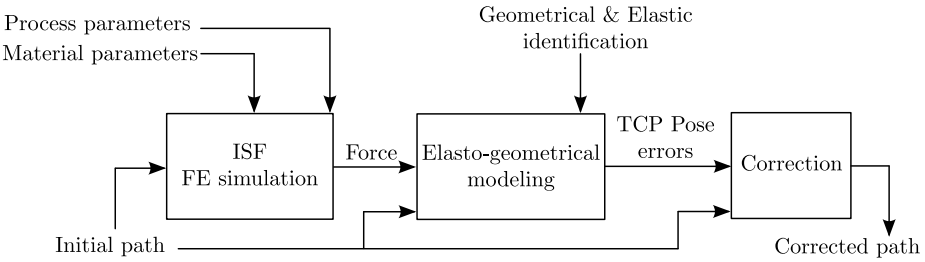

Figure 20: Post-processor scheme

The forming foces are evaluated by means of a FE simulation of the process per-

formed with ABAQUS© software assuming an ideal stiff robot and a theoretical path. The values of the stiffness matrix Ks (which depend on material properties, sheet dimensions, boundary conditions of the sheet) are not explicitly calculated but are taken into account through the FE modeling. For symmetrical parts specific boundary conditions can be applied to reduce computation time. In the other cases, a full FE modeling must be adopted. The elastic model of the robot and the calculated forces are then used to estimate the TCP pose errors induced by the elastic deformations of the robot structure at each point of the theoretical path. Those errors are added to the nominal path to obtain the final corrected tool path.

5.1. Experimental validation

5.1.1. Frustum cone

To evaluate the effectiveness of this post-processor, the same frustum cone is formed with the robot applying the corrected tool path. The force magnitude needed on each point of the tool path is derived from the one predicted by the 45° pie model. The axial component is supposed to be constant during an incremental step. Its value is determined when the TCP crosses the middle axis of the 45° pie model. The F_x, F_y components of the xy-plane force are built using sinusoidal signal. Their amplitude varies along the trajectory in function of the maximum value computed by the FE during an incremental step. Therefore an ideal force is computed for each point of the robot trajectory.

The absolute errors between the nominal and measured tool paths before and after correction, in the plane $(\mathbf{O}_p, \mathbf{x}_p, \mathbf{y}_p)$, are depicted in Figure 21. As one can see:

- Without correction: a significant TCP deviation can be noticed. The maximum value of the error norm is about 7 mm at the end of the trajectory and the mean value is about 3.1 mm. The error is not uniformly distributed along the path because of the direction of the resulting forces. When the force direction is mainly along $\mathbf{x}_p$ it produces resulting torques on robot joints.

- With correction: The maximum value of the error norm is about 0.9 mm and the mean value is about 0.5 mm. The final TCP error that can be observed after

the tool path compensation is mainly induced by the residual identification errors due to the elastic calibration. However, the TCP pose accuracy can be improved about 85% during the forming of this part.

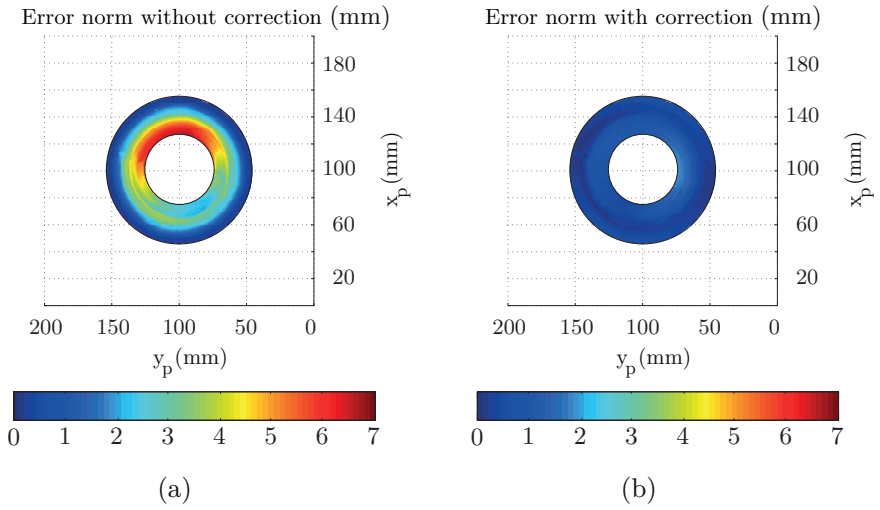

Figure 21: Norm of the error measured between the nominal and tool paths during the forming of the frustum cone (a) without correction and (b) with correction

For the final shape, the difference along the cut axis obtained respectively with the milling machine and the robot is less than 1 mm when a correction is applied against approximately 4 mm without correction (Figure 22). The shape of the frustum cone made by the robot shows an inward bulging of the unprocessed bottom central area with or without compensated path (Figure 22) whereas this phenomenon is not observed for milling machine made parts (Figure 7). As explained in Belchior et al. [2013], this effect is due to the non-symmetrical behavior of the robot during a loop of the tool path. Because the correction is not exactly the same for the points close to the $\mathbf{x}_p$ axis and for the ones close to the $\mathbf{y}_p$ axis, it causes this geometrical error. Despite this, these experimental results show the method relevance.

5.2. Twisted pyramid

By using the same procedure, a twisted pyramid is formed with the same aluminum alloy sheet. Its non-symetrical geometry will confirm the robustness of both the process FE analysis and the elastic calibration of the FANUC robot (Figure 23). The tool path

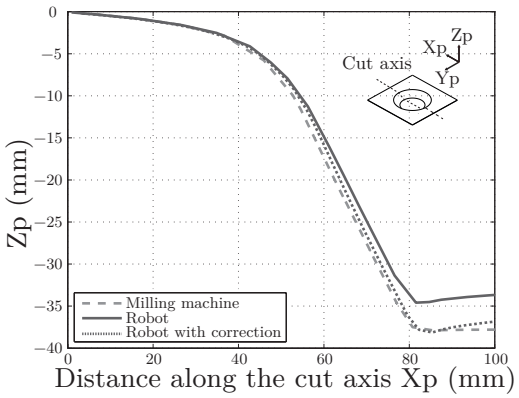

Figure 22: Measurement of the final shapes along the cut axis

consists of constant z levels (Figure 24) with an incremental step size value $\Delta_z = 1\ mm$ per loop. For this geometry, the more realistic FE modelling (Model 2) with a Voce law is directly used to compute the tool forces. Due to its non-symmetrical geometry a full model is adopted leading to an increase of the computation time (240 hours). A CAD program is directly used to compute the tool path for the simulation. The FEA gives the predicted axial and radial forces for each point of this tool path. The elastic model is then directly employed to compute the compensated tool path.

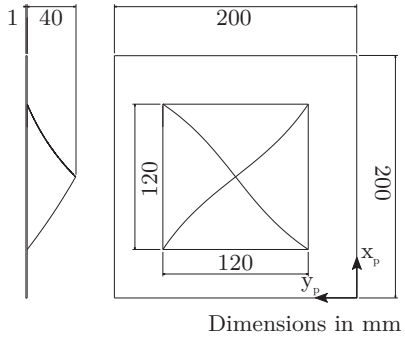

Figure 23: Geometry of the twisted pyramid

The absolute errors between the nominal and measured tool paths before and after correction given in the user frame R_p are depicted in Figure 25. The following comments can be made:

- Without correction: a significant TCP deviation can be observed. The maximum

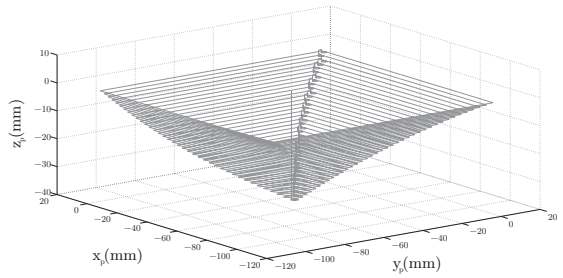

Figure 24: Target tool path of the twisted pyramid - constant z levels - Δ_z=1 mm

value of the error norm is about 6 mm at the end of the trajectory and the mean value is about 3 mm. The non-symmetry of the part implies the non-symmetry of the error. This phenomenon is explained by the various inclinations of the four faces of the twisted pyramid. It leads to modifications of the direction of the resulting forces during the path and then robot torque values.

- With correction: the pose accuracy is considerably improved. The maximum value of the error norm is about 1 mm and the mean value is about 0.6 mm. The effect of the inclination of each face of the pyramid is well compensated thanks to the good prediction of the FE forming forces (Figure 26) and to the realistic identification of the elastic behavior of the FANUC robot structure. The final TCP error after the tool path compensation is mainly induced by the residual identification errors after the elastic calibration. They introduce a difference between the predicted and measured forces which grows up with the incremental step size value (Figure 26). For more readability the presented forces are given as an average per loop. Nevertheless, the reduction of the TCP pose error compared to the milling machine results is about 80% during the forming of this part.

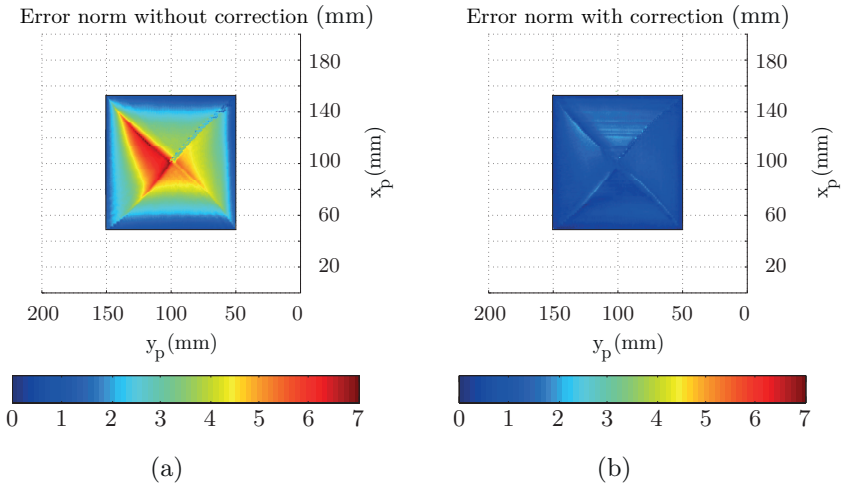

Figure 25: Norm of the error measured between the target and tool paths during the forming of the twisted pyramid (a) without correction and (b) with correction

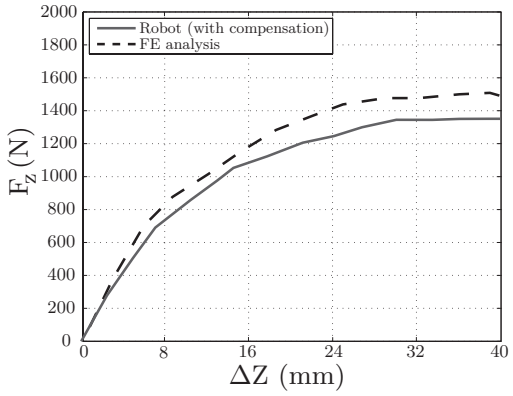

Figure 26: Measured and predicted forces (F_z) on the twisted pyramid

6. General conclusion

In this paper a correlation between numerical and experimental forces of a SPIF operation was performed. The prediction accuracy of the force needed to form a classical frustum cone was improved with the study of three influent parameters: finite element type, boundary conditions and hardening law. With Model 1, brick elements have been used to model accurately the TTS. An improvement of 30% of the force prediction has been obtained compared to the Model 0 built with the classical hypotheses of the literature. With Model 2, a more realistic clamping system with pressure areas applied on

the contact zone between the sheet and the blank holder has been defined. This modelling has increased the accuracy of the force prediction of 55% compared to Model 1. Based on Model 2, the influence of the hardening law (Ludwick or Voce) has been evaluated. A better correlation with experiments has been obtained using the Voce law instead of the Ludwick law. Using the more realistic FE modelling to compute forces, the coupling approach Machine/Process was applied to correct the tool path errors of RISF operations. The frustum cone and a non-symmetrical part (a twisted pyramid) were formed with this methodology. The experimental results show the method relevance since the errors due to the unstiffness of the serial robot for the both formed parts have been reduced with approximately 80%.

R. Aerens, P. Eyckens, A. Van Bael, and J.R. Duflou. Force prediction for single point incremental forming deduced from experimental and fem observations. International Journal of Advanced Manufacturing Technology, 46:969–982, 2010. doi: http://dx.doi.org/10.1007/s00170-009-2160-2.

J.M. Allwood and A.E. Shouler, D.R. andTekkaya. The increased forming limits of incremental sheet forming processes. Key Eng Mater, 344:621?628, 2007.

J.M. Allwood, O. Music, A. Raithatha, and Duncan S.R. Closed-loop feedback control of product properties in flexible metal forming processes with mobile tools. Annals of CIRP, 58(1):287–290, 2009. doi: http://dx.doi.org/10.1016/j.cirp.2009.03.065.

Julian M. Allwood and Daniel R. Shouler. Generalised forming limit diagrams showing increased forming limits with non-planar stress states. International Journal of Plasticity, 25(7):1207 – 1230, 2009. doi: http://dx.doi.org/10.1016/j.ijplas.2008.11.001.

G. Ambrogio, I. Costantino, L. De Napoli, and L. Filice. Influence of some relevant process parameters on the dimensional accuracy in incremental forming : a numerical and experimental investigation. Journal of Materials Processing Technology, 154:501–507, 2004. doi: http://dx.doi.org/10.1016/j.jmatprotec.2004.04.139.

552 G. Ambrogio, J. Duflou, L. Filice, and R. Aerens. Some considerations on force trends
553 in incremental forming of different materials. AIP Conference Proceedings, 907(1):
554 193–198, 2007. doi: http://dx.doi.org/10.1063/1.2729510.

555 J. Belchior, M. Guillo, E. Courteille, M. Maurine, L. Leotoing, and D. Guines. Off-
556 line compensation of the tool path deviations on robotic machining: Application to
557 incremental sheet forming. Robotics and Computer Integrated Manufacturing, 29:
558 58–69, 2013. doi: http://dx.doi.org/10.1016/j.rcim.2012.10.008.

559 P. Bigras, M. Lambert, and C. Perron. New formulation for an industrial robot
560 force controller: Real-time implementation on a kuka robot. IEEE International
561 Conference on Systems, Man and Cybernetics, pages 2794–2799, 2007. doi:
562 10.1109/ICSMC.2007.4413645.

563 C. Bouffioux, C. Henrard, J. Gu, J. Duflou, A.M. Habraken, and H. Sol. Development
564 of an inverse method for identification of materials parameters in the single point
565 incremental forming process. IDDRG, 2007. doi: http://hdl.handle.net/2268/23550.

566 A. Bres, B. Monsarrat, L. Dubourg, L. Birglen, C. Perron, M. Jahazi, and
567 L. Baron. Simulation of robotic friction stir welding of aerospace compo-
568 nents. Industrial Robot: An International Journal, 37:36–50, 2010. doi:
569 10.1108/01439911011009948.

570 Carlos Canudas de Wit, Georges Bastin, and Bruno Siciliano. Theory of Robot Control.
571 Springer-Verlag New York, Inc., Secaucus, NJ, USA, 1st edition, 1996. ISBN
572 3540760547.

573 D. Deblaise, X. Hernot, and P. Maurine. A systematic analytical method for
574 pkm stiffness matrix calculation. In IEEE International Conference on Robotics
575 and Automation, pages 4213–4219, Orlando, Florida, USA, may 2006. doi:
576 10.1109/ROBOT.2006.1642350.

577 S. Diot, D. Guines, A. Gavrus, and E. Ragneau. Forming Process of a 5083 Aluminium
578 Alloy. Constitutive Model Covering a Large Range of Temperature. International
579 Journal of Forming Processes, 9:167–168, 2006.

J. Duflou, Y. Tunçkol, and R. Aerens. Force analysis for single point incremental forming. Key Eng Mater, 344:543?550, 2007a.

J. Duflou, Y. Tunçkol, A. Szekeres, and P. Vanherck. Experimental study on force measurements for single point incremental forming. Journal of Materials Processing Technology, 189(103):65–72, 2007b. doi: http://dx.doi.org/10.1016/j.jmatprotec.2007.01.005.

C. Dumas, S. Caro, S. Garnier, and B. Furet. Joint stiffness identification of six-revolute industrial serial robots. Robotics and Computer-Integrated Manufacturing, 27:881–888, 2011. doi: http://dx.doi.org/10.1016/j.rcim.2011.02.003.

W.C Emmens and A.H van den Boogaard. An overview of stabilizing deformation mechanisms in incremental sheet forming. Journal of Materials Processing Technology, 209(8):3688–3695, 2009. doi: http://dx.doi.org/10.1016/j.jmatprotec.2008.10.003.

P. Eyckens, J. Del-lero Moreau, J. Duflou, A. Van Bael, and P. Van Hoote. MK Modelling of sheet formability in the incremental sheet forming process, taking into-account through-thickness shear. International Journal of Material Forming, pages 379–382, 2009. doi: http://dx.doi.org/10.1007/s12289-009-0458-0.

P. Flores, L Duchêne, C Bouffioux, T Lelotte, C Henrard, N Pernin, A Van Bael, S He, J Duflou, and A.M. Habraken. Model identification and fe simulations: Effect of different yield loci and hardening laws in sheet forming. International Journal of Plasticity, 23:420–429, 2007. doi: 10.1016/j.ijplas.2006.05.006.

L. Giraud-Moreau, A. Cherouat, J. Zhang, and H. Borouchaki. Comparison between an advanced numerical simulation of sheet incremental forming using adaptive remeshing and experimental results. Key Enfineering Materials, 554–557:1375–1381, 2013. doi: 10.4028/www.scientific.net/KEM.554-557.1375.

C. Henrard, C. Bouffioux, P. Eyckens, H. Sol, J. Duflou, A. Van Bael, P. Van Houte, L. Duchêne, and A.M. Habraken. Forming forces in sin-

gle point incremental forming: prediction by finite element simulations, validation and sensivity. Computational mechanics, 47:573–590, 2011. doi: http://dx.doi.org/10.1007/s00466-010-0563-4.

J. Jeswiet, JR. Duflou, and A. Szekeres. Forces in single point and two point incremental forming. Adv Mater Res, 6-8:449–456, 2005.

W. Khalil and E. Dombre. Modeling, Identification and Controls of Robots. Hermes Penton Ltd, 2nd edition, 2002.

S. Marie and P. Maurine. Elasto-geometrical modelling of closed-loop industrial robots used for machining applications. IEEE International Conference on Robotics and Automation, pages 1294–1300, may 2008. doi: 10.1109/ROBOT.2008.4543382.

H. Meier, B. Buff, R. Laurischkat, and V. Smukala. Technology increasing the part accuracy in dieless robot-based incremental sheet metal forming. CIRP Annals - Manufacturing Technology, 58:233–238, 2009a. doi: 10.4028/www.scientific.net/KEM.410-411.159.

H. Meier, R. Laurischkat, C. Bertsch, and S. Reese. Prediction of path deviation in robot based incremental sheet metal forming by means of an integrated finite element - multy body system model. Key Engineering Materials, 410–411:365–372, 2009b. doi: 10.4028/www.scientific.net/KEM.410-411.365.

H. Meier, R. Laurischkat, and J. Zhu. A model based approach to increase the part accuracy in robot based incremental sheet metal forming. AIP Conference Proceedings, 1315:1407–1412, 2011. doi: 10.1063/1.3552383.

O. Music and J.M. Allwood. The use of spatial impulse responses to characterise flexible forming processes with mobile tools. Journal of Materials Processing Technology, 212(5):1139–1156, 2012. doi: http://dx.doi.org/10.1016/j.jmatprotec.2011.12.018.

A. Petek, K. Kuzman, and J. Kopac. Forces and deformations analysis of in-

cremental sheet metal forming. Proceedings of the 11th CAM3S conference, Gliwice-Zakopane, Poland, 2005.

M. Rauch, J-Y. Hascoet, Hamann J-C., and Y. Plenel. Tool path programming optimization for incremental sheet forming applications. Computer-Aided Design, 41 (12):877–885, 2009. doi: http://dx.doi.org/10.1016/j.cad.2009.06.006.

J. Verbert, R. Aerens, H. Vanhove, E. Aertbeliën, and J.R. Duflou. Obtainable accuracies and compensation strategies for robot supported spif. Key Engineering Materials, 410 - 411:679–687, 2009. doi: 10.4028/www.scientific.net/KEM.410-411.679.

L. Vihtonen, A. Puzik, and T. Katajarinne. Comparing two robot assisted incremental forming methods: incremental forming by pressing and incremental hammering. International Journal of Material Forming, 1:1207–1210, 2008. ISSN 1960-6206. doi: 10.1007/s12289-008-0158-1.

C. Zhang, L. Leotoing, D. Guines, and E. Ragneau. Experimental and numerical study on effect of forming rate on AA5086 sheet formability. Materials Science and Engineering: A, 527:967–972, 2010. doi: http://dx.doi.org/10.1016/j.msea.2009.09.013.